# Electronic properties of epitaxial $La_{1-x}Sr_xRhO_3$ thin films

Juan Jiang,[1,*,†] Alex Taekyung Lee,[1,*] Sangjae Lee,[2] Claudia Lau,[2] Min Li,[3] Tor M. Pedersen,[4] Chong Liu,[5,6] Sergey Gorovikov,[4] Sergey Zhdanovich,[5,6] Andrea Damascelli,[5,6] Ke Zou,[5,6] Frederick J. Walker,[1] Sohrab Ismail-Beigi,[1] and Charles H. Ahn[1,2]

[1]*Department of Applied Physics, Yale University, New Haven, Connecticut 06511, USA*
[2]*Department of Physics, Yale University, New Haven, Connecticut 06511, USA*
[3]*Materials Characterization Core, Yale West Campus, West Haven, Connecticut 06516, USA*
[4]*Canadian Light Source, Inc., 44 Innovation Boulevard, Saskatoon SK S7N 2V3, Canada*
[5]*Department of Physics & Astronomy, University of British Columbia, Vancouver BC V6T 1Z1, Canada*
[6]*Quantum Matter Institute, University of British Columbia, Vancouver BC V6T 1Z4, Canada*

(Received 9 January 2021; revised 23 April 2021; accepted 26 April 2021; published 25 May 2021)

We report on the synthesis and electronic properties of epitaxial perovskite $La_{1-x}Sr_xRhO_3$ thin films. Thin films with a Sr content ranging from $x = 0$ to 0.5 have been grown using molecular beam epitaxy. Transport and x-ray photoemission spectroscopy data reveal an insulator-metal-insulator transition, accompanied by a *p*- to *n*-type carrier change observed in Hall measurements. Combined with theoretical calculations, we find that the addition of Sr does not directly dope carriers into the conduction band, but rather induces localized Rh 4*d* states within the $LaRhO_3$ band gap. The bandwidth of the impurity band increases with Sr content, eventually causing the valence band (VB) and the localized Rh 4*d* band to overlap, which explains the first insulator-to-metal transition occurring at $x = 0.35$. For Sr content $x > 0.4$, possible cation ordering results in an increase of the gap between the VB and the Rh 4*d* band, leading to the second metal-to-insulator transition. We map out the electronic phase diagram of the Sr-doped $LaRhO_3$ system and suggest strategies to engineer the electronic states in rhodate systems via delocalizing the $Rh^{3+}$ states.

DOI: 10.1103/PhysRevB.103.195153

## I. INTRODUCTION

Metal-to-insulator transitions (MITs) in transition metal oxides (TMOs) can be viewed as quantum critical points where various physical phenomena are realized via tuning parameters such as doping, strain, and pressure [1,2]. Mechanisms for MITs induced by chemical substitution include Anderson localization [3,4], which is related to disorder in the electrostatic potential seen by the carriers; Mott transition, which is related to electron correlations [5,6]; and charge disproportionation, which is due to the existence of mixed valence states [7,8]. The combination of two different MIT mechanisms has been observed in the well-studied 3*d* TMOs, such as $La_{1-x}Sr_xMnO_3$ [9–12], $La_{0.75}Sr_{0.25}VO_3$ [13], $SrTi_{1-x}Ru_xO_3$ [14–16], and the less-studied 4*d* Rh-based TMO $Sr_{2-x}La_xRhO_4$ [17]. The 4*d* TMO $SrRhO_3$ is interesting because it has been predicted to lie near a quantum critical point [18], and it is a candidate for topologically protected states, which can be realized by deliberately designing rhodium-based superlattices [19]. Moreover, due to its electronic configuration, rhodium-based double perovskites have been predicted to host unusual electronic and magnetic properties, such as ferromagnetic half-metallic states in Cr-Rh and Mn-Rh compounds and antiferromagnetic states in Fe-Rh compounds [20].

However, due to the challenges in preparing a single-crystalline phase of rhodates, measurements of their properties are lacking. Polycrystalline samples of $La_{1-x}M_xRhO_3$ ($M$ = Ca, Sr, and Ba) have been studied which exhibit a paramagnetic behavior [21] and a semiconducting-to-metal transition, which occurs at $x = 0.3$ in $La_{1-x}Sr_xRhO_3$ systems [22]. Synthesis of $SrRhO_3$ thin films has been done with the pulsed laser deposition technique, where a C-type antiferromagnetic ground state, distinct from the bulk paramagnetic metallic ground state, is observed due to a modification of octahedral rotations by the substrate [23]. As a 4*d* TMO system with moderate electron correlation strength and moderate spin-orbit coupling (SOC), one might expect to observe new electronic states in rhodate thin films, starting with the perovskite band insulator $LaRhO_3$ (LRO), and modifying its electronic states using A-site substitution and epitaxial strain.

Here, we report the growth of $La_{1-x}Sr_xRhO_3$ ($x = 0-0.5$; LSRO) thin films on $LaAlO_3$ (001) (LAO) and $SrTiO_3$ (001) (STO) substrates by molecular beam epitaxy (MBE). *In situ* reflection high-energy electron diffraction (RHEED) and atomic force microscopy (AFM) confirm the high crystalline quality of the MBE-grown thin films. X-ray diffraction (XRD) and x-ray photoemission (XPS) results show the systematic change of lattice parameter due to Sr doping, consistent with increasing Sr occupation on the A-site. An insulator-metal-insulator transition is observed in the doping range from $x = 0$ to 0.5, where a first insulator-to-metal transition takes place at $x = 0.35$ and is accompanied by a carrier type change from *p* to *n*. Another unexpected MIT transition happens at $x = 0.45$

*These authors contributed equally to this work.
†jjiangcindy@gmail.com

 

in which the carriers remain *n* type. Our theoretical calculations predict that both electron-electron interactions and SOC effects are necessary to understand the electronic structure. The addition of Sr leads to the formation of an impurity state in the $La_{1-x}Sr_xRhO_3$ thin films, consisting of localized holes on Rh sites. As the Sr content is increased, the bandwidth of the impurity state increases to a point where it overlaps with the valence band (VB) and induces a metallic state.

## II. EXPERIMENTAL AND THEORETICAL METHODS

High-quality single-crystalline LSRO thin films on both LAO (001) and STO (001) substrates were grown in an oxygen plasma-assisted MBE system with a base pressure of $\sim 1\times10^{-10}$ Torr. The substrates are pre-annealed under $O_2$ plasma with a base pressure of $5\times10^{-6}$ Torr at 500 °C for half an hour to achieve clean surfaces. The La, Sr, and Rh metals were codeposited in an oxygen environment with an oxygen partial pressure of $3.5\times10^{-6}$ Torr. The substrate temperature during growth was 700 °C. The metal fluxes were calibrated using a quartz crystal microbalance to determine the relative stoichiometry before growth and to ensure a growth rate of 1 monolayer/min. The film surface was monitored by *in situ* RHEED during deposition. All films reported here were grown with 30-unit cell (uc) thickness with a typical thickness ~12 nm. To prevent the formation of oxygen vacancies, the samples were cooled down to room temperature under an oxygen plasma. The samples were characterized by using XRD, AFM, XPS, and a Quantum Design Physical Property Measurement System (PPMS). The XPS spectra were collected at room temperature using a monochromatic 1486.7 eV Al K$\alpha$ x-ray source and a PHI VersaProbe II x-ray photoelectron spectrometer with 0.47 eV resolution. The energy scale was calibrated using Cu $2p_{3/2}$ (932.67 eV) and Au $4f_{7/2}$ (84.00 eV) peaks on a clean copper plate and a clean gold foil. Synchrotron-based VB XPS was conducted on the Quantum Materials Spectroscopy Centre (QMSC) beamline at the Canadian Light Source at 10 K with a photon energy of 100 eV, with an energy resolution better than 15 meV. To avoid charging effects, the samples used for the synchrotron measurements were grown on Nb-doped STO substrates. Before the XPS measurements, the samples were annealed in $5\times10^{-6}$ Torr oxygen plasma at 500 °C for 2 h.

For the theoretical calculations, we used the projector augmented wave method [24] as implemented in the Vienna *ab initio* Simulation Package software [25]. We used the revised version of the generalized gradient approximation (GGA) PBEsol, which is a revised Perdew-Burke-Ernzerhof GGA that improves equilibrium properties [26]. We also considered SOC self-consistently, where the spin quantization axis is the *z* axis. The GGA with Hubbard *U* parameter, GGA + *U* scheme, within the rotationally invariant formalism [27] was used to improve the description of electronic interactions. The sizes of the supercells for $x = 0.0625$, 0.25, and 0.5 were 80, 20, and 20 atoms, respectively, corresponding to $2\sqrt{2}\times2\sqrt{2}\times2$, $\sqrt{2}\times\sqrt{2}\times2$, and $\sqrt{2}\times\sqrt{2}\times2$ uc, respectively. A plane-wave basis with a kinetic energy cutoff 500 eV was used. Here, $5\times5\times7$ ($x = 0.0625$) and $9\times9\times7$ ($x = 0.25$ and 0.5) k-point meshes were employed to sample the first Brillouin zone. The stress was relaxed only along the *z* axis to be below $0.02k_B$, while the in-plane lattice parameters were fixed to 3.905 Å. We used $U(\mathrm{Rh}) = 5\,\mathrm{eV}$ to fit the optical energy gap of $LaRhO_3$ on STO substrates (1.3 eV) [28].

## III. RESULTS

The high crystallinity of the MBE-grown LSRO thin films is revealed by the AFM, RHEED, and XRD measurements in Fig. 1. Topographic images and the RHEED patterns along the [100] directions of 30-uc-thick LRO films grown on STO and LAO are shown in Figs. 1(a) and 1(b), respectively. Step terraces are visible in the AFM images with a single unit cell step height, with a root mean square root roughness <6 Å. The sharp and well-ordered RHEED patterns also indicate the growth of single-crystalline epitaxial thin films. The phase purity is further confirmed by XRD measurements shown in Figs. 1(c) and 1(d) for $x = 0$ and 0.5 thin films grown on STO and LAO, respectively. The LSRO thin films covering the entire doping range ($x = 0 - 0.5$) investigated here were grown under the same growth conditions, and all the thin films showed comparable quality (see Supplemental Material for the characterization data of the films [29]). The out-of-plane lattice parameter *c* can be determined from the XRD $\theta$-$2\theta$ scan [Figs. 1(c) and 1(d)]. We find that *c* increases from 3.98 Å ($x = 0$) to 4.00 Å ($x = 0.5$) on STO and from 3.98 Å ($x = 0$) to 4.03 Å ($x = 0.5$) on LAO with increasing Sr content, which is consistent with Sr replacing La in the perovskite structure. The reciprocal space maps (RSMs) around the substrate (103) reflections were performed on the samples. The results for $x =$ 0 and 0.5 on both substrates are shown in Fig. 1(e). For the films grown on STO substrates, the film peak and the substrate Bragg peak are aligned along the in-plane reciprocal space (H) direction, indicating that the film is coherently strained to the substrate. In contrast, for the films grown on LAO substrates, film peaks are well separated from the substrate peaks in both H and L directions, indicating the films are fully relaxed from the LAO substrate. The in-plane lattice parameter *a* can be determined from the RSM data to be 3.91 Å ($x = 0$) and 3.89 Å ($x = 0.5$) on LAO, while for the thin films grown on STO, the in-plane lattice constant is 3.905 Å through the entire doping range. The lattice constants *a* and *c* as a function of Sr concentration are displayed in the Supplemental Material [29]. From the similar lattice parameters for the films grown on LAO and STO, we expect to observe similar physical properties for the samples grown on the two substrates.

We performed XPS experiments to determine the chemical compositions of the thin films. Figure 2(a) presents XPS data for $x = 0.05$, 0.3, and 0.5 thin films. The characteristic peaks of all the elements are resolved (except for $x = 0.05$, where the Sr peak is too weak to be clearly resolved), and the peak ratio between La 3*d* and Sr 3*d* decreases, indicating the successful incorporation of Sr. The VBs were measured with 100 eV photons after cleaning the sample under oxygen plasma [Fig. 2(b)]. The LRO sample shows insulating behavior with an insulating band gap that is 0.54 eV, which is consistent with the band insulator behavior stemming from the $4d^6$ electronic configuration of LRO. As we dope Sr, the film becomes more metallic with a 0.05 eV band gap for $x = 0.3$. However, the $x = 0.5$ sample shows a band gap ~1.1 eV according to the VB XPS data, which is unexpected, since

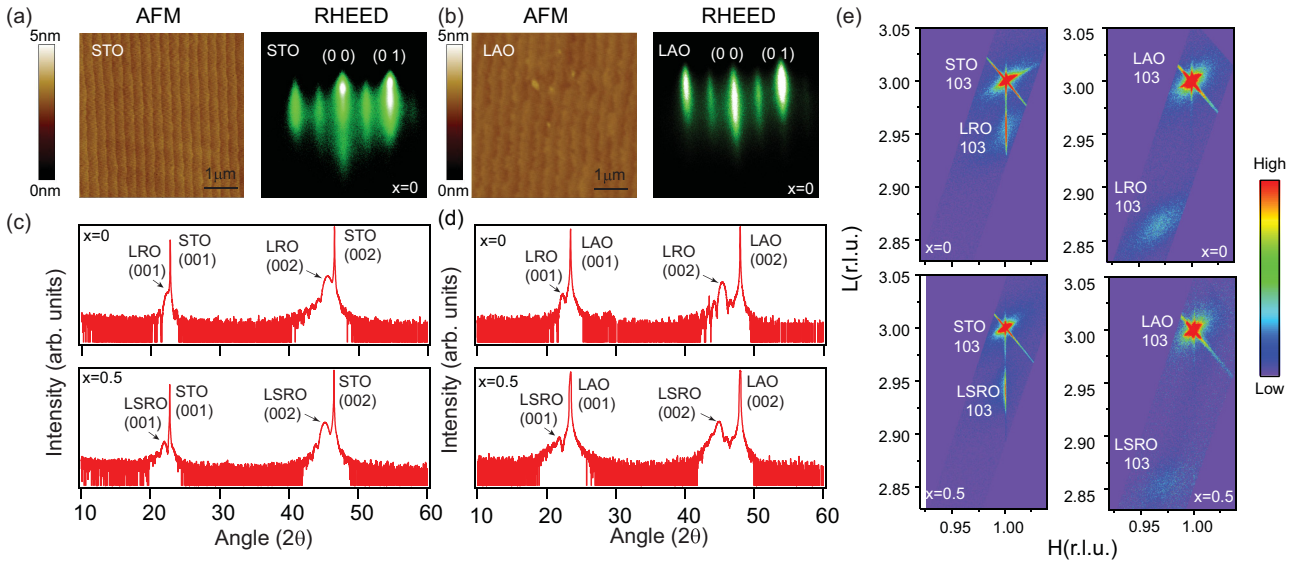


FIG. 1. Characterization of LSRO films grown on STO and LAO substrates. (a) Atomic force microscopy (AFM) topographic image (left) and reflection high-energy electron diffraction (RHEED) pattern (right) of a 30-uc-thick LRO film on STO. (b) AFM topographic image (left) and RHEED pattern (right) of a 30-uc-thick LRO film on LAO. (c) X-ray diffraction (XRD) $\theta-2\theta$ scan of 30-uc LRO (top) and $x = 0.5$ (bottom) LSRO thin films on STO. (d) XRD $\theta$-$2\theta$ scan of 30-uc LRO (top) and $x = 0.5$ (bottom) LSRO thin films on LAO. (e) Reciprocal space map (RSM) around (103) reflections of $x = 0$ and 0.5 thin films on STO (left column) and on LAO (right column).

the electronic configuration of Rh should be $4d^{5.5}$ and should result in a metallic phase in a simple band picture. Note that the gap here determined from photoemission measurements is a gap between the VB maximum and the Fermi level, which should be smaller than the insulating gap determined by the separation between the VB top and the conduction band (CB) bottom; hence, we refer to this gap as $\delta$. However, the modulation of $\delta$ for different Sr doping should still reflect the information about the insulating band gap. Thus, a unique MIT with Sr doping is identified by the VB XPS results; the origin of this unique MIT can be understood using first-principles calculations discussed below.

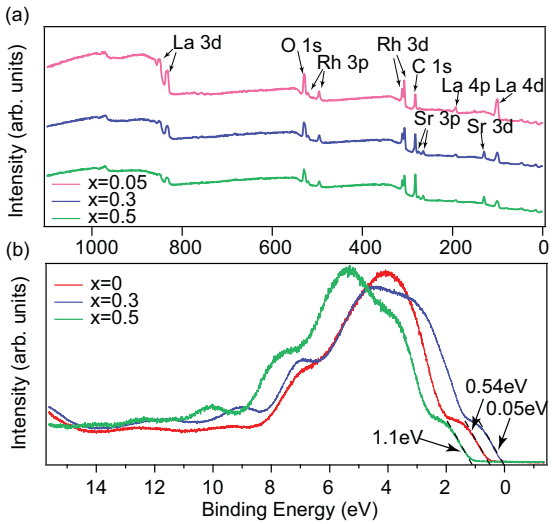


FIG. 2. Photoemission measurements as a function of Sr content. (a) Wide energy range x-ray photoemission (XPS) data of $x = 0.05$, 0.3, and 0.5 thin films. The characteristic core levels for La, Rh, Sr, and O are indicated. Note that a C 1*s* peak is also observed due to air exposure of the samples before the measurements. (b) Valence band XPS data of $x = 0$, 0.3, and 0.5 LSRO films, which indicate a band gap of 0.54, 0.05, and 1.1 eV, respectively.

To further interpret this unique MIT observed by VB XPS, the temperature-dependent resistivity (RT) of the LSRO thin films on both LAO and STO substrates is shown in Fig. 3. (The LRO data is not shown since the sample is too insulating for transport measurements.) For the LSRO samples on LAO, at lower doping ($x < 0.3$), the film is insulating, which is consistent with our results in Fig. 2(b). The LSRO thin films start to be metallic above $x = 0.35$, reflecting the first MIT in the system. Interestingly, the electrical conductivity starts to decrease at $x = 0.45$, while the RT curve shows an insulating behavior again. This is consistent with the VB XPS data of the $x = 0.5$ sample where an insulating gap of 1.1 eV is found. A similar phenomenon exists in the samples grown on STO, as shown in Figs. 3(c) and 3(d). One may notice that the precise doping level for the MIT is slightly different for the films on two substrates, which may be due to the slight difference (∼0.7%) in their lattice parameters.

To visualize which conduction channel contributes to this electronic transport behavior in LSRO thin films, we conducted room temperature Hall measurements of the samples, covering the entire doping range which can be investigated. The three-dimensional (3D) carrier densities of the thin films deducted from the Hall data are summarized in Fig. 3(e). (The data below $x = 0.2$ are missing because the sample is too insulating for Hall measurements.). The hole-type carriers dominate the charge transport in the lower doping range below $x = 0.3$. However, there is an abrupt transition from hole-type to electron-type carrier above $x = 0.3$ on both substrates, accompanied by an insulator-to-metal transition, and the carrier type remains electron type for the higher doping ranges. The experimental observations on these transport measurements are summarized in Fig. 3(f), where room temperature

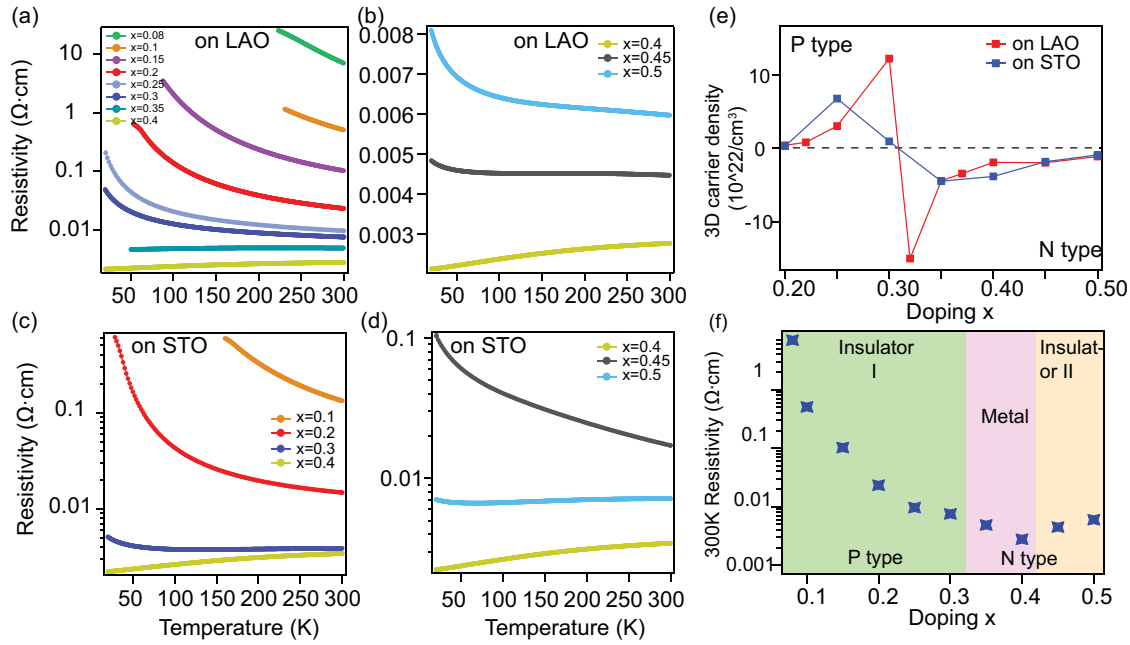


FIG. 3. Temperature-dependent resistivity (RT) as a function of Sr-doping. (a) RT curves of samples grown on LAO from $x = 0.08$ to 0.4. An insulator-to-metal transition occurs at $x = 0.35$. (b) RT curves of samples grown on LAO from $x = 0.4$ to 0.5. A metal-to-insulator transition takes place at $x = 0.45$. (c) RT curves of samples grown on STO from $x = 0.08$ to 0.4. An insulator-to-metal transition occurs at $x = 0.4$. (b) RT curves of samples grown on STO from $x = 0.4$ to 0.5. A metal-to-insulator transition takes place at $x = 0.45$. (e) Three-dimensional (3D) carrier densities of the LSRO thin films on both LAO and STO substrates. (f) Phase diagram of the LSRO thin films, showing the insulator-metal-insulator transition and a *p*-to-*n*-type carrier transition. The data plotted are extracted from the room temperature RT of the thin films grow on LAO.

RT vs Sr doping $x$ is plotted. In this phase diagram, we refer to the three different phases as insulator I, metal, and insulator II phases, respectively. In the insulator I phase, *p*-type carriers dominate the transport, while in the metal and insulator II phases, *n*-type carriers dominate the transport. Using the formula relating Hall RT to carrier density in a single-carrier model [$n = B/(R_H qd)$), where $B$ is the magnetic field, $R_H$ is the Hall resistance, $q$ is the elementary charge, the sign of $n$ is the carrier type, and $d$ is the thickness of the film], one obtains an unphysical result that the effective carrier density diverges while approaching the first MIT. This means that at least two types of carriers (e.g., electrons and holes) must be considered. The unexpected change in the Hall carrier type indicates that an electronic transition may happen above $x = 0.3$, whereas the presence of the MIT within the electron carrier type regime cannot be understood without further electronic reconstruction around the Fermi level. The origin of this unique carrier type change and how the second exotic MIT is induced is further discussed below.

## IV. DISCUSSION

We conducted first-principles calculations to better understand these MITs at $x = 0.35$ and 0.45. The calculations were performed for ordered structures with $x = 0$, 0.0625, 0.25, and 0.5, where unit cells with $a^-a^-b^+$-type octahedral tilt were used with sizes of $2\sqrt{2}\times2\sqrt{2}\times2$, $\sqrt{2}\times\sqrt{2}\times2$, and $\sqrt{2}\times\sqrt{2}\times2$, respectively (80, 20, and 20 atoms per cell). As shown in Figs. 4(a)–4(d), adding Sr results in the formation of an impurity band (IB), which sits in between the VB and CB, instead of simply doping mobile holes into the system. This IB is composed of localized holes on $Rh^{3+}$ sites. For small Sr content $x = 0.0065$, the IB is narrow with a bandwidth W = 71 meV, with negligible overlap between neighboring $Rh^{3+}$ sites. The bandgap $\Delta$, which is determined by the distance between the VB top and the IB bottom, is ~0.404 eV. Charge carriers are induced by thermal electron-hole excitation so that, at low Sr content, the more highly mobile holes in the VB dominate the Hall resistance, and the conduction is apparently *p* type. Once the amount of dopant is increased, the bandwidth of the IB is increased to W = 0.451 eV for $x = 0.25$, and this results in a smaller bandgap $\Delta = 0.104$ eV. The increased hopping of electrons in the IB means that the electrons start to contribute to the Hall resistance, and the coexistence of both hole and electron transport causes an apparent increase in the 3D carrier concentration. This trend with Sr content is shown schematically in Fig. 4(f), which shows that, for Sr content of $x \sim 0.4$, the IB band bottom overlaps with the top of the VB, resulting in a metallic state which occurs experimentally at $x = 0.35$. At this point, the calculations suggest that the bandwidth of the IB is large enough that the Hall resistance changes signs, and electrons become the dominant charge carrier.

The use of a small and ordered $\sqrt{2}\times\sqrt{2}\times2$ uc containing only 4 Rh atoms (20 atoms total) for $x = 0.25$ and 0.5 means that effects of disorder, e.g., Anderson localization, are not present in the calculations since the A-site dopants are placed in an ordered manner. To study the qualitative effects of disorder, we consider random configurations of Sr atom dopants at $x = 0.5$ in the $2\sqrt{2}\times2\sqrt{2}\times2$ uc containing 16 Rh

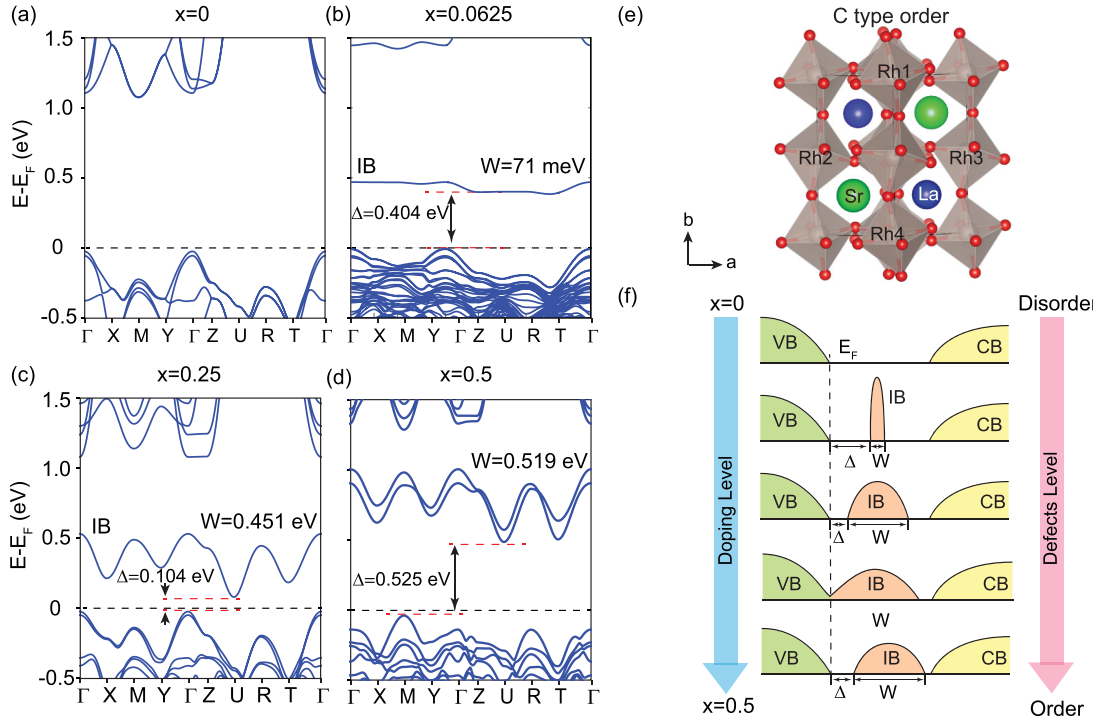


FIG. 4. (a)–(d) Theoretical calculations of the band structures of $x = 0$, 0.0625, 0.25, and 0.5 LSRO thin films, respectively. (e) Schematic of a C-type ordering of the Sr and La cations. (f) Schematic of the change in band structures and electronic states with different doping levels.

atoms (80 atoms total). We compute the electronic spectra for five random configurations and confirm that $LaRhO_3$ is insulating with a clear band gap near the Fermi level for the five cases, indicating that the insulating properties are not due to Anderson localization but rather to the localization of holes (see Figs. S5 and S6).

The measured transport and VB XPS data for $x = 0.5$ are explained qualitatively by a tendency of the Sr and La cations to order in a *C*-type configuration [Fig. 4(e)]. For a fully ordered structure, the band gap $\Delta$ increases dramatically to 0.525 eV, as shown in Fig. 4(d). This observation agrees with the experimental data, indicating that the ordering of the defects with doping may play a role in the reentrant transport behavior shown in Fig. 3(f). While we do not observe Bragg reflections in XRD due to *C*-type cation ordering, the tendency predicted by theory is enough to widen the energy gap. In addition, the band structure calculation qualitatively fits the VB XPS measurements of the bandgap.

## V. SUMMARY

We find using a combination of theory and experiment that the addition of Sr to the band insulator $LaRhO_3$ adds localized $Rh^{3+}$ bound states within the band gap. For small doping concentrations, a narrow IB forms, and the system behaves as a standard *p*-type doped material. Higher levels of doping lead to a surprising change of carrier type to *n* type, coincident with an insulator-to-metal transition: theory and experiment show this is due to the IB intersecting the VB, as the former widens. Further Sr doping leads to another transition to an *n*-type insulator: theory suggests that, at high doping levels, a structural ordering of the cations associated with a charge disproportionation among the Rh sites leads to an opening of a gap between the VB and the IB. These unexpected transitions point to the complex and interesting physics of the rhodate system. Future strategies for delocalizing the $Rh^{3+}$ states that may lead to higher conductivity include structural modifications via substitution of other alkaline rare-earth cation dopants.

## ACKNOWLEDGMENTS

Work at Yale is supported by the U.S. Department of Energy, Office of Science, Office of Basic Energy Sciences, under Award Number DE-SC0019211. We thank the Yale Center for Research Computing for guidance and use of the research computing infrastructure. This work also used the Extreme Science and Engineering Discovery Environment (XSEDE), which is supported by National Science Foundation grant number ACI-1548562, by using computer time on the Comet super- computer as enabled by XSEDE allocation MCA08X007. Synchrotron-based XPS measurements were performed at the Canadian Light Source, a national research facility of the University of Saskatchewan, which is supported by the Canada Foundation for Innovation (CFI), the Natural Sciences and Engineering Research Council (NSERC), the National Research Council (NRC), the Canadian Institutes of Health Research (CIHR), the Government of Saskatchewan, and the University of Saskatchewan. This research was undertaken thanks in part to funding from the Max Planck-UBC-UTokyo Centre for Quantum Materials and the Canada First Research Excellence Fund, Quantum Materials and Future Technologies Program. This project is also funded by the Canada Research Chairs Program (A.D.), and the CIFAR Quantum Materials Program (A.D.).

[1] M. Imada, A. Fujimori, and Y. Tokura, Metal-insulator transitions, Rev. Mod. Phys. **70**, 1039 (1998).

[2] A. T. Lee and C. A. Marianetti, Structural and metal-insulator transitions in rhenium-based double perovskites via orbital ordering, Phys. Rev. B **97**, 045102 (2018).

[3] P. W. Anderson, Absence of diffusion in certain random lattices, Phys. Rev. **109**, 1492 (1958).

[4] F. Evers and A. D. Mirlin, Anderson transitions, Rev. Mod. Phys. **80**, 1355 (2008).

[5] A. Georges, G. Kotliar, W. Krauth, and M. J. Rozenberg, Dynamical mean-field theory of strongly correlated fermion systems and the limit of infinite dimensions, Rev. Mod. Phys. **68**, 13 (1996).

[6] N. F. Mott, The basis of the electron theory of metals, with special reference to the transition metals, Proc. Phys. Soc. A **62**, 416 (1949).

[7] J. Cheng, K. E. Kweon, S. A. Larregola, Y. Ding, Y. Shirako, L. G. Marshall, Z. Y. Li, X. Li, A. M. dos Santos, M. R. Suchomel, K. Matsubayashi, Y. Uwatoko, G. S. Hwang, J. B. Goodenough, and J. S. Zhou, Charge disproportionation and the pressure-induced insulator-metal transition in cubic perovskite $PbCrO_3$, Proc. Natl. Acad. Sci. USA **112**, 1670 (2015).

[8] S. Johnston, A. Mukherjee, I. Elfimov, M. Berciu, and G. A. Sawatzky, Charge Disproportionation Without Charge Transfer in the Rare-Earth-Element Nickelates as a Possible Mechanism for the Metal-Insulator Transition, Phys. Rev. Lett. **112**, 106404 (2014).

[9] A. Seeger, P. Lunkenheimer, J. Hemberger, A. A. Mukhin, V. Y. Ivanov, A. M. Balbashov, and A. Loidl, Charge carrier localization in $La_{1-x}SrMnO_3$ investigated by AC conductivity measurements, J. Phys.: Condens. Matter **11**, 3273 (1999).

[10] A. Urushibara, Y. Moritomo, T. Arima, A. Asamitsu, G. Kido, and Y. Tokura, Insulator-metal transition and giant magnetoresistance in $La_{1-x}Sr_xMnO_3$, Phys. Rev. B **51**, 14103 (1995).

[11] M. B. Salamon and M. Jaime, The physics of manganites: Structure and transport, Rev. Mod. Phys. **73**, 583 (2001).

[12] E. Dagotto, T. Hotta, and A. Moreo, Colossal magnetoresistant materials: The key of the phase transition, Phys. Rep. **344**, 1 (2001).

[13] T. M. Dao, P. S. Mondal, Y. Takamura, E. Arenholz, and J. Lee, Metal-insulator transition in low dimensional $La_{0.75}Sr_{0.25}VO_3$ thin films Appl. Phys. Lett. **99**, 112111 (2011).

[14] K. W. Kim, J. S. Lee, T. W. Noh, S. R. Lee, and K. Char, Metal-insulator transition in a disordered and correlated $SrTi_{1-x}Ru_xO_3$ system: Changes in transport properties, optical spectra, and electronic structure, Phys. Rev. B **71**, 125104 (2005)..

[15] J. Kim, J.-Y. Kim, B.-G. Park, and S.-J. Oh, Photoemission and x-ray absorption study of the electronic structure of $SrRu_{1-x}Ti_xO_3$, Phys. Rev. B **73**, 235109 (2006).

[16] R. Gupta, I. N. Bhatti, and A. K. Pramanik, Critical behavior in itinerant ferromagnet $SrRu_{1-x}Ti_xO_3$, J. Magn. Magn. Mater. **465**, 193 (2018).

[17] J. Kwon, M. Kim, D. Song, Y. Yoshida, J. Denlinger, W. Kyung, and C. Kim, Lifshitz-Transition-Driven Metal-Insulator Transition in Moderately Spin-Orbit-Coupled $Sr_{2-x}La_xRhO_4$, Phys. Rev. Lett. **123**, 106401 (2019).

[18] D. J. Singh, Prospects for quantum criticality in perovskite $SrRhO_3$, Phys. Rev. B **67**, 054507 (2003).

[19] J.-M. Carter, V. V. Shankar, M. A. Zeb, and H.-Y. Kee, Semimetal and topological insulator in perovskite iridates, Phys. Rev. B **85**, 115105 (2012).

[20] A. Halder, D. Nafday, P. Sanyal, and T. Saha-Dasgupta, Computer predictions on Rh-based double perovskites with unusual electronic and magnetic properties, npj Quantum Mater. **3**, 17 (2018).

[21] T. Nakamura, T. Shimura, M. Itoh, and Y. Takeda, Magnetic and electric properties of $La_{1-x}M_xRhO_3$ ($M$ = Ca, Sr, and Ba): Hole doping of $4d$ orbitals of $Rh^{3+}$ with low spin configuration, J. Solid State Chem. **103**, 523 (1993).

[22] T. A. Mary and V. Varadaraju, Orthorombic to tetragonal and semiconductor-metal transitions in the $La_{1-x}Sr_xRhO_3$ system, J. Solid State Chem. **110**, 176, (1994).

[23] J. Nichols, S. F. Yuk, C. Sohn, H. Jeen, J. W. Freeland, V. R. Cooper, and H. N. Lee, Electronic and magnetic properties of epitaxial $SrRhO_3$ films, Phys. Rev. B **95**, 245121 (2017).

[24] P. E. Blöchl, Projector augmented-wave method, Phys. Rev. B **50**, 17953 (1994).

[25] G. Kresse and D. Joubert, From ultrasoft pseudopotentials to the projector augmented-wave method, Phys. Rev. B **59**, 1758 (1999).

[26] J. P. Perdew, A. Ruzsinszky, G. I. Csonka, O. A. Vydrov, G. E. Scuseria, L. A. Constantin, X. Zhou, and K. Burke, Restoring the Density-Gradient Expansion for Exchange in Solids and Surfaces, Phys. Rev. Lett. **100**, 136406 (2008).

[27] A. I. Liechtenstein, V. I. Anisimov, and J. Zaanen, Density-functional theory and strong interactions: Orbital ordering in Mott-Hubbard insulators, Phys. Rev. B **52**, R5467(R) (1995).

[28] M. Nakamura, Y. Krockenberger, J. Fujioka, M. Kawasaki, and Y. Tokura, Perovskite $LaRhO_3$ as a $p$-type active layer in oxide photovoltaics, Appl. Phys. Lett. **106**, 072103 (2015).

[29] See Supplemental Material at http://link.aps.org/supplemental/10.1103/PhysRevB.103.195153 for the characterization data of the films.